Dynamic tensile mechanisms and constitutive relationship in CrFeNi medium entropy alloys at room and cryogenic temperatures

Kai Wang,[1] Xi Jin,[1] Yong Zhang,[2] Peter K. Liaw,[3] and Junwei Qiao[1,*]

[1]*College of Materials Science and Engineering, Taiyuan University of Technology, Taiyuan 030024, China*

[2]*State Key Laboratory for Advanced Metals and Materials, University of Science and Technology Beijing, Beijing 100083, China*

[3]*Department of Materials Science and Engineering, The University of Tennessee, Knoxville, Tennessee 37996, USA*

(Received 29 June 2021; accepted 5 November 2021; published 30 November 2021; corrected 9 December 2021)

Harsh service conditions in aerospace, defense and military, and other fields are calling for materials with excellent mechanical properties to undergo extreme deformation (such as elevated and cryogenic temperatures and high strain rates) without sustaining damage while retaining high strength. Outstanding mechanical properties of high or medium entropy alloys (MEAs) render them potential candidates. In this paper, as the temperature decreases, a breakthrough of the strength-ductility tradeoff is achieved in a CrFeNi MEA with partially recrystallized face-centered cubic phases, together with body-centered cubic (BCC) precipitates. At a strain rate of 3000 s^{-1}, the yield strength (YS) is increased from 920 MPa at 298 K to 1320 MPa at 77 K, while the uniform elongation (UE) increases by 28.5%. This phenomenon also occurs at quasistatic tension. Under low-temperature loading, nanotwins are popularly activated due to the decreased stacking fault energy with decreasing temperatures. A positive strain-rate dependent YS arises owing to the contributions from the short-range dislocation obstacles, BCC phases, and refined grains. High-density dislocations and BCC phases result in the degeneration of UE, especially with the increase of strain rates. Strain-rate- and temperature-dependent constitutive models were successfully established to predict the deformation behaviors of CrFeNi MEAs under such a wide range of strain rates at room and cryogenic temperatures.

DOI: 10.1103/PhysRevMaterials.5.113608

I. INTRODUCTION

Extreme conditions, such as elevated and low temperatures, high pressures, high deformation rates, and strong radiation, often exist in aerospace, defense and military, reactor, industrial, and other fields. With the development of these advanced industries, more and more stringent requirements for high-performance structural materials are increasingly expected. In contrast, most traditional metals and alloys face the strength-ductility tradeoff dilemma, especially under extreme conditions [1–3], and cannot meet these extreme requirements. High entropy alloys (HEAs), also known as multiprincipal element alloys or complex concentrated alloys, break through the strength-ductility tradeoff, i.e., they are simultaneously strong and ductile [3–5]. Generally, HEAs process much more metastable states than conventional dilute alloys, and thus, broader tailorable mechanical properties are available. Under extreme conditions, outstanding resistances and large tolerances to external sufferings can be popularly realized in HEAs, such as outstanding elevated [6–8] and cryogenic [9–11] temperature performances, super welding properties [12], good fatigue [13,14] and fracture resistance [4,15], and good hydrogen embrittlement [16]. These excellent properties render them the potential next generation of structural materials.

Usually, HEAs/medium entropy alloys (MEAs) with single face-centered cubic (FCC) structures show excellent ductility but relatively low strengths [17,18], while body-centered cubic (BCC) structured HEAs always display high strengths but relatively poor ductility [18]. Gratefully, if dual-phase (FCC + BCC) HEAs are properly designed, a good combination of strength and toughness may be achieved [19,20]. Herein, a duplex FCC + BCC CrFeNi MEA subjected to proper thermomechanical processing was developed.

During load-bearing services for structural materials, it is inevitable to suffer from high-speed loadings. To further promote the application of HEAs/MEAs under extreme loading, it is imperative to reveal their dynamic mechanical behavior and microscopic-deformation mechanisms. Up to now, studies have mainly focused on the dynamic compression of HEAs/MEAs [21–27]. However, the dynamic tensile behavior has been rarely investigated [3,28,29]. It should be mentioned that tension and compression asymmetry is generally present in almost all alloys [30,31]. Meanwhile, these studies have mainly focused on the dynamic deformation at room temperature, and studies on the dynamic deformation at cryogenic temperature are lacking. Therefore, it is urgently necessary to explore the dynamic tensile behavior of HEAs/MEAs, especially at cryogenic temperatures.

In this paper, the microstructural evolution and mechanical behavior of the CrFeNi MEA upon quasistatic and dynamic tensile loading (at strain rates of 2000–4000 s^{-1}) at room temperature (298 K) and cryogenic temperatures (77 K) were investigated in detail. The deformation mechanisms

*Corresponding author. Email: qiaojunwei@gmail.com

of the present MEAs with high strengths and considerable elongations under low temperatures and/or high strain rates were explored. Meanwhile, quantitatively, the strain-rate- and temperature-dependent constitutive models are exactly established to predict the deformation behavior of CrFeNi MEAs over a wide range of strain rates at room and cryogenic temperatures.

II. EXPERIMENTAL

The material used in this paper was an equiatomic MEA with a nominal composition of CrFeNi. Samples with dimensions of 80 × 22 × 2 mm were cast in a vacuum arc melting furnace with suitable copper molds, using high-purity constituent elements (purity > 99.9% wt. %). The ingots were flipped and remelted at least five times to ensure thorough mixing and chemical uniformity. As-cast plates were homogenized at 1200 °C for 2 h to eliminate the dendrite segregation and obtain a single FCC structure with equiaxed grains ∼160 μm, which has been displayed in previous work [32]. Then they were multipass cryorolled up to 70% reduction in thickness (final thickness of ∼0.6 mm) using a laboratory-scale rolling mill. During the cryorolling, the specimens were immersed in liquid N_2 for 10 min before each pass. The cryorolled sheets were subsequently annealed at 800 °C for 1 h, followed by water quenching.

Rectangular dog-bone tensile specimens for quasistatic and dynamic tensile tests were machined with the tension axis oriented along the rolling direction, and they were carefully ground down to a 2000-grit SiC paper. The gauge dimensions (width, thickness, and length) of quasistatic and dynamic tensile specimens were $4 \times 0.6 \times 10\,mm^3$ and $4 \times 0.6 \times 5\,mm^3$, respectively. Quasistatic uniaxial tensile tests were conducted at a strain rate of $1 \times 10^{-3}\,s^{-1}$ and temperatures of 298 and 77 K using an Instron 5969 testing machine. Dynamic tensile tests were carried out at strain rates of $3000\,s^{-1}$ and temperatures of 298 and 77 K using a modified split Hopkinson tensile bar apparatus. Before cryogenic temperature tests, the specimens were entirely immersed in a bath of liquid nitrogen for at least 10 min. During the entire cryogenic tension, liquid nitrogen was continuously added to ensure that the samples were completely immersed in a bath of liquid nitrogen. To investigate the strain-rate sensitivity (SRS), tensile properties at strain rates of 1×10^{-4}, 1×10^{-1}, 2000, and $4000\,s^{-1}$ were investigated at 298 K. All tests were repeated at least three times at each strain rate and temperature to confirm reproductivity.

Phase structures of samples before and after tension were recognized by x-ray diffraction (XRD) measurements on Rigaku Ultimata IV x-ray equipment, using Cu Kα radiation. The scanning rate of $4^\circ\,s^{-1}$ and the range of 20–100° were applied. The microstructures were examined using scanning electron microscopy (SEM) equipped with an electron backscatter diffraction (EBSD) on JEOL JSM-7100F field emission gun-scanning electron microscopy. The accelerated voltage of 25 kV and scanning step size of 0.3 μm were chosen to obtain EBSD data. The EBSD samples were polished with 2000-grit SiC paper and subsequently electrochemically polished using a 10% perchloric acid + 90% ethyl alcohol (volume percent) at a direct voltage of 15 V at room temperature. Transmission electron microscopy (TEM) investigations were conducted on a JEOL-2100 TEM operated at 200 kV to examine detailed structures before and after tension to reveal strain-rate- and temperature-dependent deformation mechanisms. The TEM samples were first mechanically ground to a thickness of 50 μm and then twin-jet electropolished using 10% perchloric acid + 90% ethyl alcohol (volume percent) at −25 °C, followed by Ar-ion milling to suitable thickness.

III. RESULTS

A. Microstructures

XRD patterns of as-cast and as-annealed samples are shown in Fig. 1(a). As expected, a set of BCC diffraction peaks are found after annealing at 800 °C for 1 h. The lattice constants of both FCC and BCC phases were estimated to be 0.3597 and 0.2886 nm, respectively. Figure 1(b) presents the bright-field (BF) TEM image and corresponding select-area electron diffraction (SAED) patterns of the sample before deformation. The SAED patterns further confirm an FCC + BCC duplex structure. In addition, energy diffraction spectrum point analyses were performed on the two grains indicated by the yellow arrows in Fig. 1(b), and the results are summarized in Table I. It is noted that the BCC phase is mainly enriched in Cr, while the FCC phase has an almost equal content of three elements. The volume fraction of FCC and BCC phases were counted to be ∼90 and ∼10%, respectively, based on the XRD pattern and numerous BSE maps. The Cr-rich BCC phases are also found in other Cr-containing HEAs [33–35] and stainless steels [36].

Several factors account for the availability of Cr-rich precipitates. Firstly, from the view of the average valence electron concentration (VEC), which is a well-developed parameter to predict the solid-solution phase formation in multiprincipal elements alloys, the value of VEC is 8 for current CrFeNi MEAs. As is known, VEC values of 8 and 6.8 are the critical values to distinguish the single FCC region and single BCC region, respectively [37]. Some HEAs or MEAs with VEC of 8, such as $Al_{0.8}$CoCrCuFeNi [38] and AlCuNi [38], have an FCC + BCC duplex structure. Secondly, Cr is a BCC phase stabilizer [37]. Based on calculations from the CompuTherm software (shown in Fig. S1 in the Supplemental Material [39]), for $Cr_x(FeNi)_{100-x}$ alloy systems, the maximum Cr content for a single FCC phase structure at 800 °C is 28.6 at. %. At relatively low temperatures, the solid solubility of atoms, especially the Cr atom with a higher melting point, is significantly reduced in the matrix, which easily causes the formation of Cr-rich secondary precipitates. Additionally, Cr has a higher diffusion coefficient than Fe and Ni atoms, which may facilitate its precipitation from the matrix [40]. Thirdly, partial pair correlation functions ($g_{\alpha\beta}$), which are key parameters to predict the existence of elemental preferential short-range ordering (SRO), can be used to investigate SRO in current CrFeNi MEAs [41]. The $g_{\alpha\beta}$ values from *ab initio* molecular dynamics simulations show that certain nearest-neighbor pairs, such as Cr-Cr and Cr-Fe, occur much more frequently than others (for example, Ni-Ni, Ni-Fe, and Ni-Cr) [41]. These SROs can be regarded as precursors for nucleating segregated Cr-rich phases [41]. Consequently, Cr-rich precipitates are available in the present MEA.

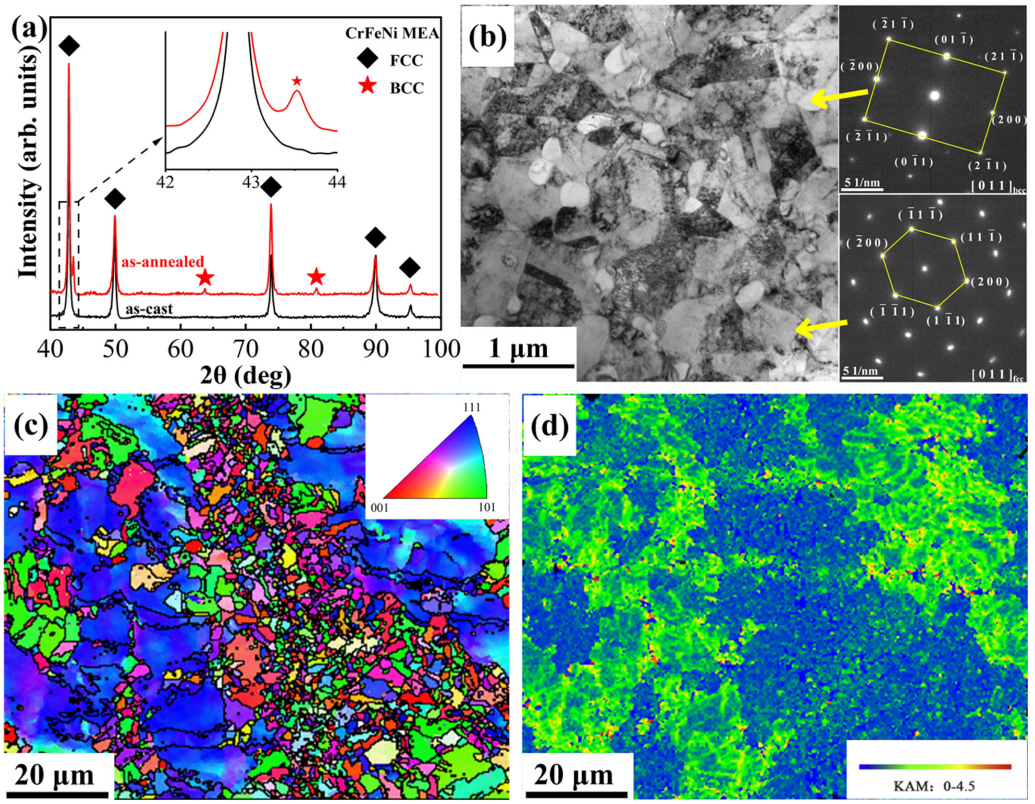

FIG. 1. Microstructures of CrFeNi medium entropy alloys (MEAs). (a) X-ray diffraction (XRD) patterns of as-cast and as-annealed samples, showing body-centered cubic (BCC) phases. (b) Bright-field transmission electron microscopy (TEM) micrographs with the corresponding select-area electron diffraction (SAED) patterns of as-annealed CrFeNi MEAs. (c) Electron backscatter diffraction (EBSD) inverse pole figure (IPF) maps of an-annealed CrFeNi MEAs, showing a heterogeneous structure, and (d) corresponding kernel average misorientation (KAM) maps.

Meanwhile, some areas with high dislocation densities are found in Fig. 1(b), which are considered nonrecrystallized zones. The heterogeneous structure was demonstrated by an inverse pole figure (IPF) of EBSD, as shown in Fig. 1(c). Both partially recrystallized regions with fine grains and coarsened nonrecrystallized grains coexist. Analogous combinations of such heterogenous structures have come about in CrCoNi MEAs [42]. The volume fraction of the recrystallized region was estimated to be ∼42% from IPF images. An average grain size of the recrystallized FCC phase is 760 nm, and that of the BCC phase is 355 nm. Moreover, the corresponding local misorientations were observed in the EBSD kernel average misorientation (KAM) map, as presented in Fig. 1(d). It indicates that the dislocation density in the nonrecrystallized regions is higher than that in the recrystallized ones.

B. Mechanical properties

Figure 2(a) exhibits the representative quasistatic and dynamic tensile engineering stress-strain curves tested at room and cryogenic temperatures, and the tensile properties are summarized in Table II. For convenience, the specimens deformed under quasistatic (10^{-3} s^{-1}, Q) and dynamic (3000 s^{-1}, D) tensile loading at room temperature (298 K) and cryogenic temperature (77 K) are referred to as Q298, Q77, D298, and D77, respectively. The dimples are popular on all the rupture surfaces, typical of ductile fracture (shown in Fig. S2 in the Supplemental Material [39]). The average yield tensile strength (YS), average ultimate tensile strength (UTS), and average uniform elongation (UE) of Q298 are 605 ± 6 MPa, 785 ± 12 MPa, and 18 ± 1%, respectively. At a constant strain rate of 10^{-3} s^{-1}, as the temperature decreases from 298 to 77 K, both the strength and ductility increase. The

TABLE I. Chemical compositions of phases for CrFeNi MEAs.

Phase	Average size	Volume fraction	Chemical composition/at. %		
			Cr	Fe	Ni
FCC	760 nm	∼90%	34.11	33.83	32.06
BCC	355 nm	∼10%	86.49	11.58	1.93

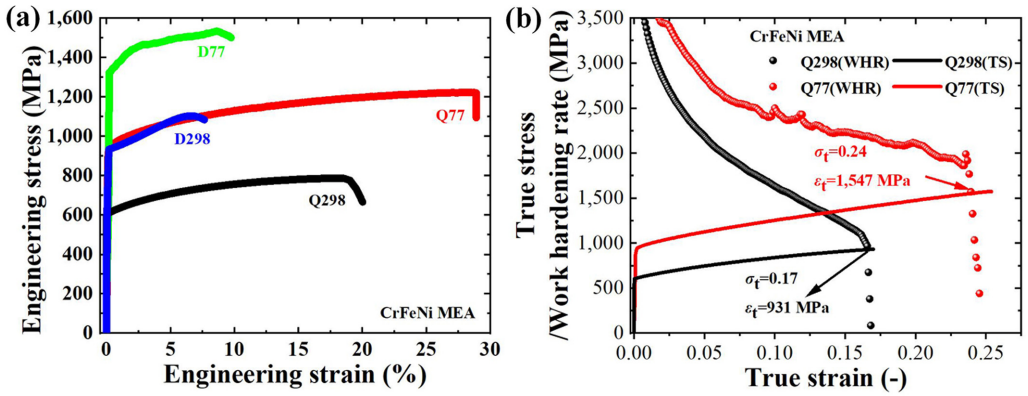

FIG. 2. (a) Quasistatic and dynamic engineering stress-strain curves tested at room and cryogenic temperatures of the CrFeNi medium entropy alloys (MEAs). The alloys both exhibit ductile dimpled structures and (b) true stress-true strain curves and work-hardening rate vs true strain curves of Q298 and Q77.

average YS and UTS are increased to 940 and 1220 MPa, respectively. Meanwhile, the UE of Q77 is 29%. This notably simultaneous improvement of strength and elongation is commonly achieved in FCC-based HEAs [5,43]. Astonishingly, the strength and ductility of D77 are increased simultaneously as compared with D298. The YS, UTS, and UE of D77 reach 1320 ± 12 MPa, 1530 ± 15 MPa, and 9 ± 1%, respectively. In brief, under a constant strain rate, the lower the tested temperature, the stronger and tougher for the current MEAs, in consistency with previous studies [4].

Figure 2(b) displays the true stress-strain curves of Q298 and Q77 specimens and the corresponding work-hardening rate (WHR) curve. Since the work-hardening fluctuation is severe under dynamic loading, it is not considered in this paper. Obviously, the WHR of the Q77 specimen is much higher than that of the Q298 one, and it is possible that there are extra strengthening mechanisms associated with the increased lattice-friction resistance at 77 K. The onset of localized deformation (plastic instability or necking) during tension could be determined by a Considére criterion, as expressed as $\frac{d\sigma}{d\varepsilon} \leqslant \sigma$ (here, σ and ε are true stress and true strain, respectively) [44]. The intersections of the WHR and true stress are plotted in Fig. 2(b). The true strain at the beginning of necking in Q298 is 0.17, while that of the Q77 is 0.24. At 77 K, the improvement of the work-hardening ability can essentially delay necking, and hence, the fracture strain is accordingly enhanced. Moreover, the enhanced work-hardening capability facilitates the increase of the UTS. The UTS of the Q77 specimen is 1575 MPa, while it is only 945 MPa in the Q298 specimen.

To illustrate the simultaneous improvement of strength and ductility in the current CrFeNi MEA, the correlations between the percentage change of YS and UE with deformation temperatures decreased from 298 to 77 K at constant strain rates of 10^{-3} or $3000\,s^{-1}$ are displayed in Fig. 3. In comparison, much more data are collected from many kinds of metals and alloys, including pure elements, stainless steels, dual-phase steels, twinning-induced plasticity (TWIP) steels, transformation-induced plasticity (TRIP) steels, titanium alloys, magnesium alloys, metallic glass matrix composites, and HEAs [26,31,45–57]. Detailed data are listed in Table S1 in the Supplemental Material [39]. Relative to other alloys, the CrFeNi MEA exhibits a higher value of the product of the change percentage of YS and the change percentage of UE. Generally, the temperature sensitivity of YS is increased as the solute concentration increases, which has been confirmed by Wu *et al.* [17]. The highest solute concentration results in a current ternary equiatomic MEA. Also, the pure BCC metals usually display greater temperature sensitivity of YS than pure FCC metals [17,48]. There are 10% (volume percent) BCC phases in the CrFeNi MEA, and consequently, the temperature sensitivity is higher than those alloys, such as $V_{10}Cr_{10}Fe_{45}Co_{35}$ with single FCC phases. Additionally, the low stacking fault energy (SFE) of the FCC matrix, calculated based on large-scale atomistic simulations, promotes the dynamic formation of deformation twins, which substantially

TABLE II. Comparison of YSs, ultimate strengths, and UEs of the CrFeNi MEAs under different conditions (σ_y: strain rate, σ_y: YS, ε_{uni}: UE, σ_{uti}: ultimate tensile stress, $\sigma_{uti} - \sigma_y$: the difference between the YS and ultimate tensile stress).

T (K)	$\dot{\varepsilon}$ (s^{-1})	σ_y (MPa)	ε_{uni} (%)	σ_{uti} (MPa)	$\sigma_{uti} - \sigma_y$ (MPa)
77	10^{-3}	940 ± 7	29 ± 2	1220 ± 10	280
	3000	1320 ± 12	9 ± 1	1530 ± 15	210
298	10^{4}	550 ± 8	21 ± 1	745 ± 6	195
	10^{-3}	605 ± 6	18 ± 1	785 ± 12	180
	10^{-1}	725 ± 9	14 ± 2	845 ± 10	120
	2000	800 ± 13	10 ± 1	1010 ± 18	210
	3000	920 ± 15	7 ± 1	1110 ± 15	190
	4000	1010 ± 10	4 ± 1	1160 ± 22	150

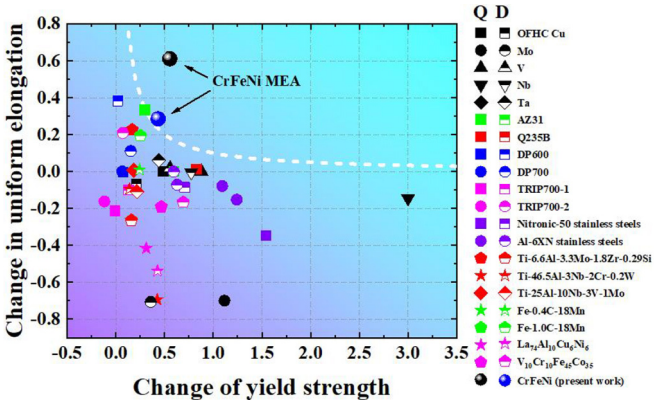

FIG. 3. Plots of change of uniform elongation (UE) and change of yield tensile strength (YS) of some conventional metals and alloys, high entropy alloys (HEAs), and metallic glass matrix composites ($V_C = \frac{V_{77}-V_{298}}{V_{77}}$).

increases the strain-hardening ability, leading to the superior tensile ductility at cryogenic temperatures [58,59].

Figure 4 shows the engineering stress-strain curves at different strain rates upon room-temperature tension, and the correspondingly measured tensile properties are summarized in Table II. The YS is almost doubled, from 550 to 1010 MPa, with an increase of the strain rate from 1×10^{-4} to $4000\,s^{-1}$, and it may be attributed to a typical strain-rate hardening effect [60,61]. However, UE is decreased from 21 to 4%, accordingly. The higher the strain rate, the stronger but the less ductility for most metals and alloys. SRS m is often employed to characterize the strain-rate effect, which is defined by the slope of the logarithmic flow stress vs the logarithmic strain rate. The inset presents the SRS of CrFeNi MEAs, which can be classified into two distinct regions: I and II. Accordingly, the SRS of the two regions, m_s (quasistatic) and m_d (dynamic), are calculated to be 0.0371 and 0.33968, respectively. Apparently, the strain-rate strengthening is more significant upon dynamic tension, which is common in FCC-based HEAs [3,62].

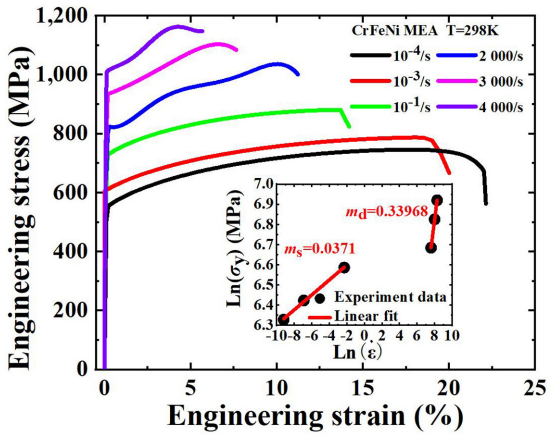

FIG. 4. Engineering stress-strain curves of current CrFeNi medium entropy alloys (MEAs) at different strain rates. The inset shows the variation of yielding strengths with strain rates at two distinct regions for CrFeNi MEAs.

IV. DISCUSSION

A. Deformation mechanisms

1. Dislocations

Figure 5 displays the EBSD KAM maps of FCC phases in Q298, Q77, D298, and D77. Corresponding average KAM values and the density of geometrically necessary dislocations (GNDs) are summarized and displayed in Figs. 5(e) and 5(f), respectively. The average KAM values of Q298, Q77, D298, and D77 are calculated to be 0.786, 1.68, 0.763, and 0.455. The density of GNDs can be estimated using the relationship of the density of GNDs ρ^{GND} and misorientation angle θ (i.e., the KAM value), and it is expressed as follows [63]:

$$\rho^{GND} = \frac{2\theta}{\mu b}, \tag{1}$$

where b is the magnitude of the Burgers vector ($b = \frac{\sqrt{2}}{2} \times a = 0.254$ nm), a is the lattice constants of FCC phases calculated from XRD patterns. Here, μ is the unit length ($\mu = 10^{-5}$ m) [63]. The densities of GNDs in Q298, Q77, D298, and D77 are estimated to be 6.14×10^{14}, 1.32×10^{15}, 6.01×10^{14}, and $3.58 \times 10^{14}\,m^{-2}$, respectively. Obviously, the fractured Q77 samples have the highest density of GNDs, which gives a clue that the contribution of GNDs to the work hardening of Q77 is the largest. It agrees with the greatest value in Q77 of $\sigma_{uti} - \sigma_y$.

The TEM analyses of dislocation structures in Q298, Q77, D298, and D77 are presented in Fig. 6. Tangles of randomly distributed dislocations are found from the matrix of four samples, and no dislocation cell appears. There are many dislocations piling up at the boundaries of FCC and BCC phases. Slip lines can be found to intersect in Cr-rich BCC precipitates, especially in samples deformed plastically at 77 K. Slip-slip interactions (forest hardening) can further contribute to growing stress levels with straining [64]. Similar slipping is uncovered in FCC + BCC duplex alloys, including $Al_{0.6}$CoCrFeNi [62] and $Al_{0.5}$FeCoCrNiHEAs [64].

2. Structure transformation

In addition, for Cr-rich alloys, such as 18Cr8Ni stainless steels, martensite transformation easily takes place upon heavily plastic deformation [65]. However, from the XRD patterns of Q298, Q77, D298, and D77 shown in Fig. S3 in the Supplemental Material [39], similar phase transformation is absent during the whole tension, which may be attributed to the weight fraction of Ni being much higher than that in the traditional austenitic stainless steel, while Ni is a austenite stabilizer [66]. Additionally, Zhao *et al.* [67] and Ming *et al.* [68] found the presence of amorphous bands in deformed CrMnFeCoNi and $Cr_{26}Mn_{20}Fe_{20}Co_{20}Ni_{14}$HEAs. In this paper, numerous TEM analyses rule out amorphous phases induced by shear banding. Significant dislocation accumulation in a constrained region inside shear bands raises the free energy of the original FCC phase to a point higher than that of amorphous phases. Then the energy difference drives transformation [68]. The critical dislocation density for the transformation is proportional to the SFE [67]. The SFE of the current MEA is calculated to be $65.85\,mJ\,m^{-2}$ (298 K) and $43.30\,mJ\,m^{-2}$ (77 K; the detailed calculation can be

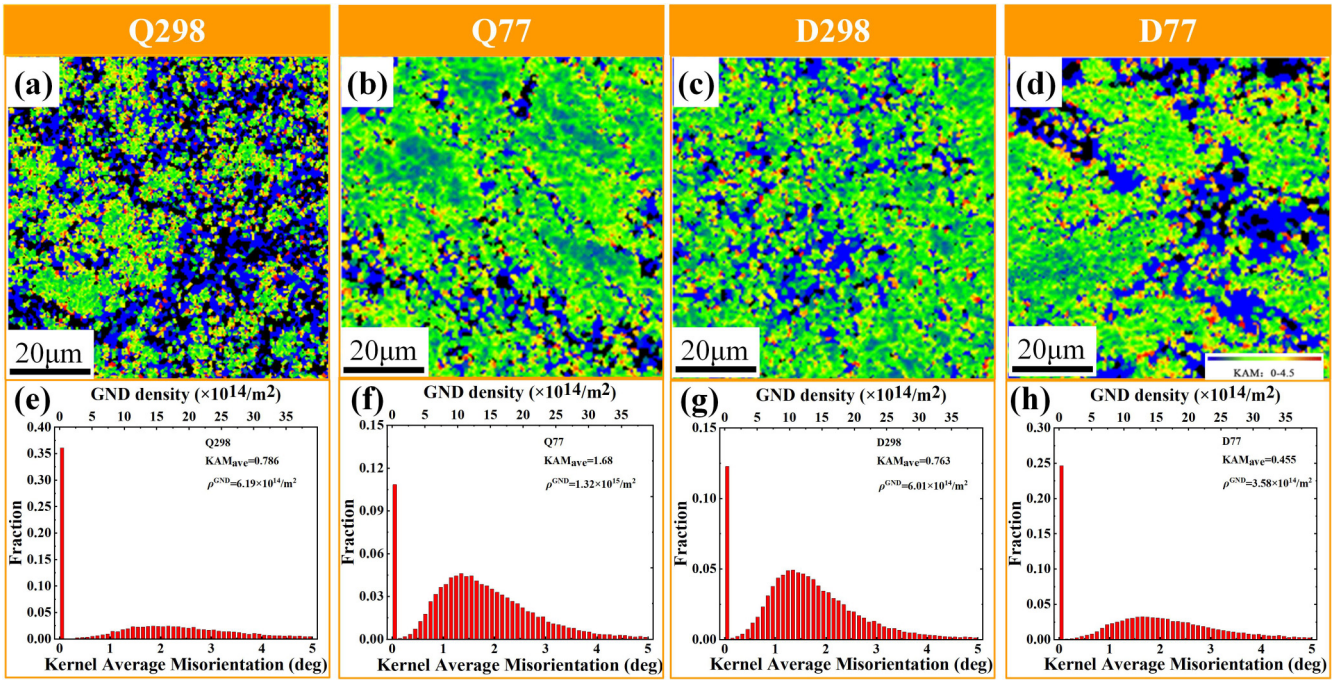

FIG. 5. Dislocations with grains after fracture. (a)–(d) Electron backscatter diffraction (EBSD) kernel average misorientation (KAM) maps of Q298, Q77, D298, and D77, respectively. (e)–(h) The statistical histograms of the KAM/geometrically necessary dislocation (GND) density evolution of Q298, Q77, D298, and Q77, respectively. The average values are shown in the figure.

found in the Supplemental Material [39,59,69–78]), which is more than several times that of $Cr_{26}Mn_{20}Fe_{20}Co_{20}Ni_{14}$HEAs [68]. In other words, the critical dislocation density for phase transformation in the current CrFeNi MEA is several times that of the $Cr_{26}Mn_{20}Fe_{20}Co_{20}Ni_{14}$HEA. Thus, amorphization is absent in the current CrFeNi MEA.

3. *Twinning*

Figure 7 shows the EBSD band contrast maps with Σ3 twin boundaries, which were marked in yellow. Surprisingly, twin boundaries popularly exist in all four samples. Owing to the limit resolution of EBSD and the thickness of deformation twins being as small as a few nanometers, individual

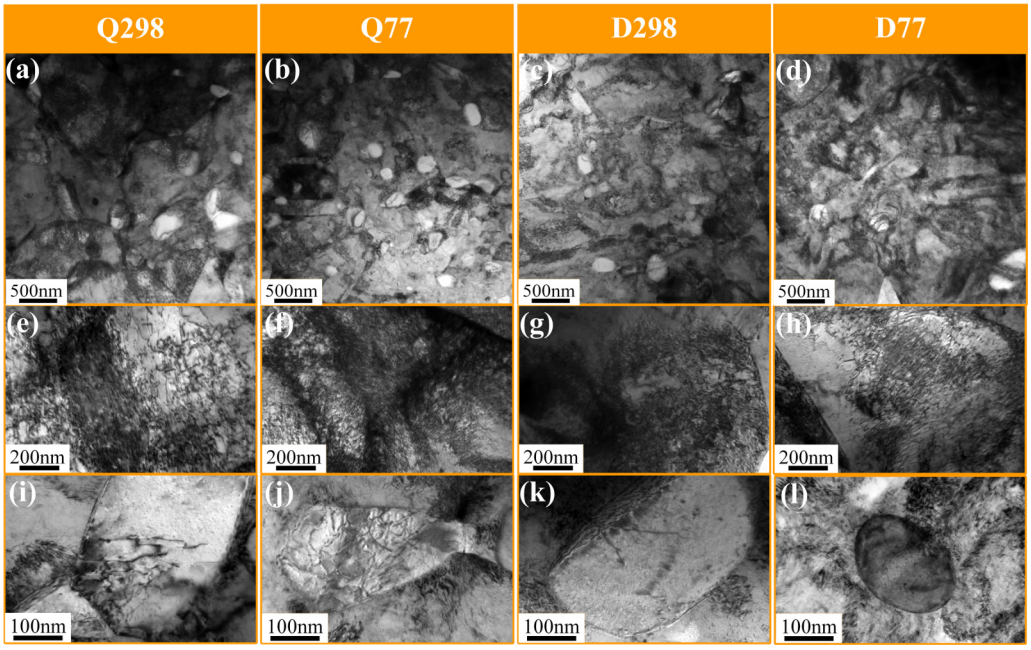

FIG. 6. Dislocation structures of the alloys after fracture. (a)–(d) Bright-field transmission electron microscopy (TEM) images of Q298, Q77, D298, and Q77, respectively. (e)–(h) Dislocations in the face-centered cubic (FCC) matrix of Q298, Q77, D298, and Q77, respectively. (i)–(l) Dislocations in the Cr-rich body-centered cubic (BCC) precipitates of Q298, Q77, D298, and Q77, respectively.

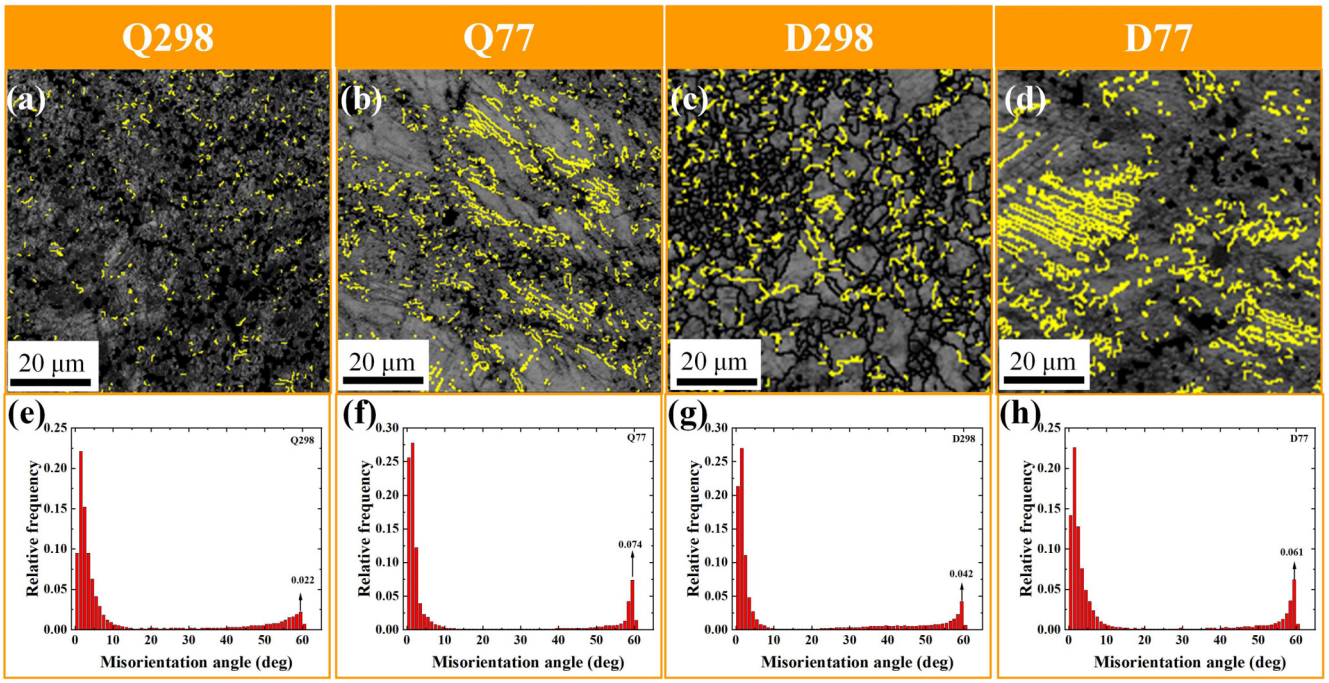

FIG. 7. Twins of the alloys after fracture. (a)–(d) Electron backscatter diffraction (EBSD) band-contrast maps with Σ3 twin boundaries of Q298, Q77, D298, and Q77, respectively. (e)–(h) The statistical histogram of misorientation angle of Q298, Q77, D298, and Q77, respectively.

twins cannot be powerfully captured by EBSD technique. In other words, the twin boundaries observed in the band-contrast maps may be deformation-twin bundles (DTBs) [3]. The areal fractions of the DTBs in the fracture samples are estimated to be 2.2, 7.4, 4.2, and 6.1% using the corresponding relative frequency of misorientation angles, respectively. Alternatively, the TEM technique with a better spatial resolution was adopted to identify individual twins, as presented in Fig. 8. There are no parallel bands available in Q298, and thus, the twin boundaries from EBSD band-contrast maps can be caused by special grain orientation, as happens in TWIP steels [79]. Thus, the deformation twins have nearly zero effect on the WHRs during quasistatic deformation at 298 K. In contrast, profuse parallel bands are found in Q77, D298, and D77. Both high-resolution TEM and SAED maps (almost the same for three conditions) uncover that these parallel bands are DTBs. The average twin thicknesses are estimated to be 2.5, 11.6, and 5.3 nm for D298, Q77, and D77, respectively, based

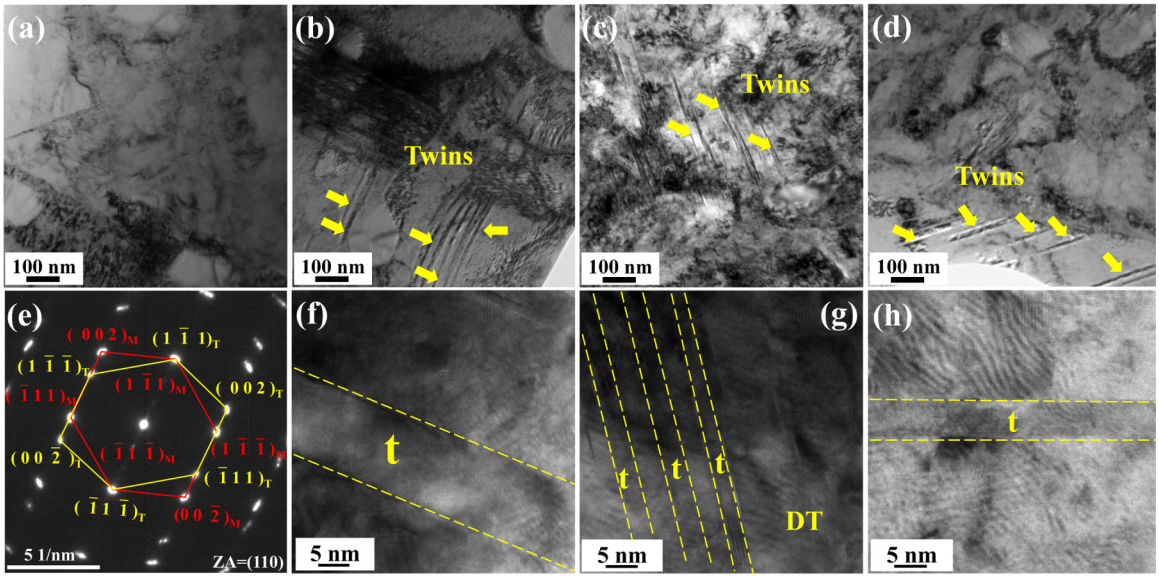

FIG. 8. Twins of the alloys after fracture. (a)–(d) Bright-field transmission electron microscopy (TEM) images of Q298, Q77, D298, and Q77, respectively. (e) Select-area electron diffraction (SAED) map of parallel bands in (b). The SAED maps of parallel bands in (c) and (d) are similar. (f)–(h) Twins in the face-centered cubic (FCC) matrices of Q77, D298, and Q77, respectively.

on numerous high-resolution TEM maps. The areal fractions of the matrix and twin lamellae in the DTBs are almost the same, ∼50%. Combining the results from EBSD and TEM observations, the twin fractions in D298, Q77, and D77 are finally evaluated to be 2.1, 3.7, and 3.1%, respectively.

It is well established that either a decrease in temperatures or an increase in strain rates could facilitate twinning relative to slipping due to restricted dislocations [80–82]. For instance, in $V_{10}Cr_{15}Mn_5Fe_{35}Co_{10}Ni_{25}$HEAs, a slip-TWIP transition with decreasing temperatures was discovered [83]. Laplanche *et al.* [84] proposed that twins could be generated during successively plastic straining at room temperature, when the stress was larger than the critical stress for twinning. Thus, the critical stress required for twinning governs the initial twinning. It has been demonstrated that the predicted values of the critical twinning stress for CoCrFeNi HEAs could be well calculated, using the Steinmetz equation [71]. According to Steinmetz *et al.* [85], the critical stress required for twinning is expressed as

$$\sigma_T = \frac{M\gamma_{\mathrm{SFE}}}{3b_p} + \frac{3Gb_pM}{L_0}, \tag{2}$$

where σ_T is the critical stress for twinning, γ_{SFE} is the SFE, M is the Taylor factor (taken as 3.06), and b_p is the Burgers vector of the partial dislocations with $b_p = 0.254$ nm [86]. The values of SFE at 298 and 77 K are substituted into Eq. (2), and the critical stresses required for twinning are obtained. The critical twinning stress for the FCC phase of CrFeNi MEAs at 298 K is 1069 MPa, while the UTS of Q298 and D298 are 932 and 1178 MPa, respectively. In other words, upon tensile straining at 3000 s^{-1}, the twinning takes place at a true plastic strain of 3.55%.

Generally, the higher the strain rate, the larger velocity for dislocation movement. Hence, dislocation pileups easily come about and further result in localized stress concentration that acts as effective nucleation sites for deformation twins. Woo *et al.* [87] have found that a large amount of stacking faults/twins in CoCrNi MEAs at high strain rates increases the stacking fault probability and in turn drives the decrease of the SFE. The critical twinning stress for the FCC phase at 77 K is 978 MPa, and the UTS of Q77 and D77 are 1573 and 1666 MPa, respectively. Meanwhile, the YS of Q77 and D77 are 940 and 1320 MPa, respectively. Consequently, the twinning occurs at a true plastic strain of 0.7% for Q77. However, for D77, the true stress reaches the critical twinning stress at the beginning of plastic deformation. The theoretical calculations agree well with the above observations that twinning is lacking in Q298, while deformation twins are widely found in Q77, D298, and D77. Therefore, at 77 K, the plasticity of FCC phases is partly originated from deformation twins. Dislocation slip can even occur in BCC phases to coordinate further straining caused by deformation twins generated in the FCC phases. It is concluded that the generation of deformation twins may promote the work-hardening capability [88]. Nanoscale twin boundaries could act as effective barriers against dislocation movement and reduce the mean free path of dislocation glide like grain boundaries, known as the dynamic Hall-Petch effect. The activation of profuse twin systems at 77 K leads to a significant improvement of the work-hardening capacity for the current CrFeNi MEA. Furthermore, according to the Considére criterion [44], twin-induced hardening can delay plasticity instability to a higher strain. Therefore, CrFeNi MEAs have higher tensile strengths and larger elongations at 77 K than that at 298K.

4. Excellent mechanical properties upon dynamic loadings

For CrFeNi MEAs, the yield strengths (YSs) were significantly increased upon dynamic loading since the dislocation motion becomes popular under high strain-rate loading [3,26]. The fracture strain decreases upon dynamic tension since the stress concentration may happen from the heterogeneous distribution of dislocations, originating from insufficient recovery upon low-temperature annealing. Similar results have been revealed in the prestrained AISI 301LN2B metastable austenitic stainless steels [89]. The UE of this kind of steel with high-density dislocations is decreased as the strain rate increases, while samples with few dislocations show an opposite trend.

Apart from the heterogeneous dislocation structure, the complex microstructure may affect the strain-rate-dependent plasticity. For instance, for single-phase $V_{10}Cr_{10}Fe_{45}Co_{30}Ni_5$ [90] and CoCrFeNi [91] FCC HEAs, the strength is significantly enhanced, and meanwhile, the UE remains almost unchanged upon dynamic loading since successive twinning is accompanied. For conventional BCC metals and alloys, a positive strain-rate effect exists in the YS, but a negative one occurs in plasticity [92]. In comparison, the HEAs with an FCC + BCC + B2 structure [22,28] from dynamic compression display a strength-ductility tradeoff. Compared with the quasistatic compression, the strength of HEAs with a BCC1 + BCC2 structure [24] upon dynamic compression is improved, and the UE is reduced. These results verify analogous strain-rate-dependent strength or plasticity in HEAs/MEAs, as found in traditional BCC metals and alloys.

To sum up, the twinning in the FCC phases usually leads to an increased UE, but the BCC phases usually decrease it. Therefore, high-density dislocations, together with BCC phases within the FCC matrix, reduce UEs in D298 and D77.

Based on the above analysis, the microstructure evolution subjected to the thermomechanical treatment and plastic straining for the current CrFeNi MEAs are schematically depicted in Fig. 9. The initial microstructure after homogenization is composed of coarse FCC grains with few dislocations. After rolling and annealing, the heterogeneous structure appears, which consists of the coarse uncrystallized grains, recrystallized dislocation-free FCC grains, and recrystallized dislocation-free BCC grains. Before loading, the dislocations are mainly concentrated in the coarse uncrystallized grains, and twinning is not activated. Subjected to quasistatic tension at 298 K, dislocations are generated within the recrystallized FCC grains. It indicates that slipping prevails during quasistatic and room-temperature tension. After dynamic tension at 298 K, due to strong and positive SRS, the strength of D298 is much higher than that of Q298, and it is easy to reach the critical twinning stress. Twinning takes place in the recrystallized FCC grains. Upon tension at 77 K, a lower SFE results at cryogenic temperatures, which can promote continuous twinning (nucleating at initial dislocation pileups). Twinning prevails within the recrystallized FCC

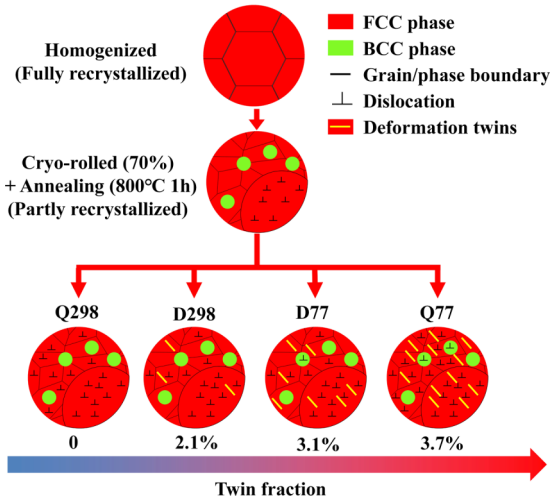

FIG. 9. Schematic diagrams of microstructural evolution under different conditions.

grains even at low strains (<1%). Meanwhile, dislocations dominate within the recrystallized BCC grains upon heavily plastic deformation. Since brittle BCC phases may result in stress concentration, the UE is lower at high strain rates. As a result, a premier failure happens for D77. Both the volume fraction of twins and dislocation density of Q77 are higher than those of D77, as there is insufficient time for dislocations or twins to develop.

B. SRS

The values of quasistatic SRS (m_s) as well as dynamic SRS (m_d) of some HEAs/MEAs together with many metals and alloys under tension are listed in Fig. 10 and Table SII in the Supplemental Material [3,21,25,28,29,39,46,48,49,51,52,62,82,93–100]. Meanwhile, some quasistatic and dynamic SRSs of HEAs and MEAs under compression are also included in Fig. 10. Obviously, the m_s and m_d of HEAs, MEAs, and steels are remarkably higher than those of pure FCC metals and dilute FCC alloys, which may originate from strong short-range dislocation obstacles [3]. For HEAs and MEAs, the dislocation obstacles are popular since strong

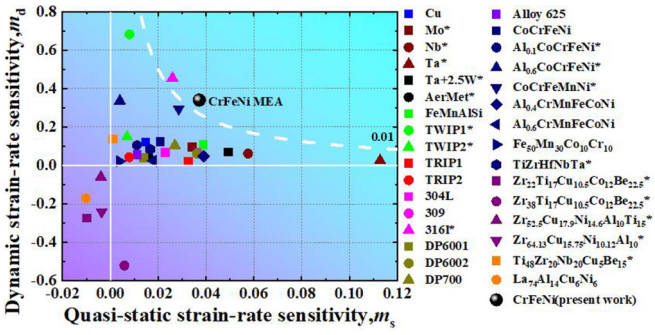

FIG. 10. Plots of quasistatic strain-rate sensitivity (SRS; m_s) and dynamic SRS (m_d) of some conventional alloys, high entropy alloys (HEAs), medium entropy alloys (MEAs), and metallic glasses (*: data from compression experiments).

Peierls-Nabarro barriers (i.e., lattice friction resistance) are available, including severe lattice distortions [101–103] and nanoscale inhomogeneities, including coclusters and/or short-range chemical orders [104,105].

From Fig. 10, the present CrFeNi MEA has higher m than most HEAs and MEAs, which may be attributed to the ultrafine grains of recrystallized microstructures and BCC phases, both of which have been proven to significantly increase SRS. For example, Komarasamy *et al.* [106] found that the SRS reduced as the grain size increased. BCC-structured Nb [48] and Ta [49] display higher m than FCC metals under quasistatic loading. According to these studies, it is reasonable to infer a high m for the current MEA. However, compared with 316L stainless steels, the m_d of current CrFeNi MEA is lower [96]. Here, m_d of 316L stainless steels are obtained from dynamic compression at 2700, 4200, 5600, 6900, and 7500 s^{-1} [96], while currently investigated strain rates are of 2000–4000 s^{-1}, much lower than those for 316L stainless steels. As demonstrated above, more rapid enhancement for the YS, i.e., high m_d, may arise upon high-speed loading due to the dislocation drag. Additionally, tension-compression asymmetry exists frequently in most alloys [30,31]. Previous studies have revealed that the value of m from compression is higher than that from tension [107,108]. As a result, a lower m_d of the current CrFeNi MEAs come into being than 316L stainless steels.

Furthermore, for metallic glasses (amorphous alloys) with disordered structures, since the high strain rate would dramatically increase adiabatic heating within shear layers and the thermal softening plays a leading role, the YS was negatively correlated with the strain rate [109]. In contrast, by introducing crystalline phases, metallic glass matrix composites show a positive SRS when the dislocation-strengthening mechanism is dominant. Hence, a moderate positive SRS is achieved in these kinds of composites [110].

C. Constitutive relationship

1. Strain-rate-dependent YS

According to different dislocation velocities, mechanisms governing plastic deformation can be divided into thermally activated dislocation motion, dislocation drag, and relativistic effects mechanisms [111]. Thermally activated dislocation motion mechanisms usually govern plastic deformation at low strain rates. For a pure FCC Cu, the dislocation drag should be considered only if the strain rate is $> 24\,000\ s^{-1}$ [112]. Recent investigations on the constitutive relation of CoCrFeNi HEAs upon dynamic tension ($\dot{\varepsilon} \geqslant 3000\ s^{-1}$) have been done [3]. A modified Zerilli-Armstrong (Z-A) model, which is a physically based constitutive relationship, based on a thermally activated dislocation motion theory, is well established by introducing the dislocation drag [3]. It is necessary here to testify the improved model in current duplex MEAs. A Z-A model is expressed as [113]

$$\sigma_y = \beta_0 \varepsilon^{1/2} \exp\left(-\beta_1 T + \beta_2 T \ln \dot{\varepsilon}\right) + \sigma_0, \tag{3}$$

where β_0, β_1, and β_2 are material constants, ε is the yield strain, and it takes values of 0.002, and T is the absolute

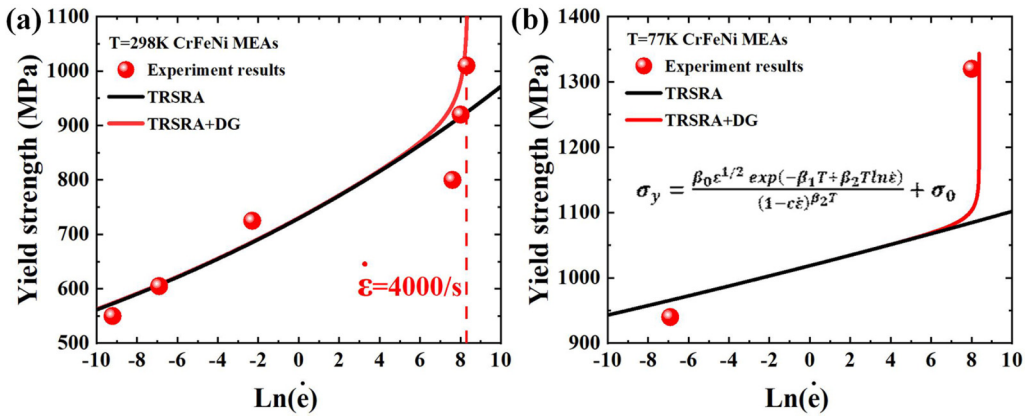

FIG. 11. (a) Modeling the strain-rate dependence of the yield tensile strength (YS) at 298 K. The black and red threads are thermal activation equation predictions without and with dislocation drag, respectively. (b) The comparison of experimental and predicted YSs at 77 K with dislocation drag.

temperature, and it is 298 K for room-temperature tension. Here, σ_0 is the athermal stress and taken as the grain-boundary strengthening for the current CrFeNi MEA. Here, we approximately adopted the value of a strengthening coefficient k_y from CoCrNi alloys, and it is 265 MPaμm$^{1/2}$ [44]. As is listed above, the average grain size of FCC phases in recrystallized zones (volume fraction of ~60%) is ~760 nm. Accordingly, the value σ_0 is calculated to be 182.4 MPa. The experimental results from different strain rates are used to determine the parameters in Eq. (3), and the values of β_0, β_1, and β_2 from best fitting are 4.85×10^5 MPa, 1.92×10^{-3} K^{-1}, and 1.23×10^{-4} K^{-1}, respectively. The strain-rate effects of σ_y in CrFeNi MEAs under quasistatic loading can be well described via Eq. (3) [see Fig. 11(a)]. However, an obvious deviation between the experimental results and theoretical predictions (black thread) comes about at a strain rate of 4000 s^{-1}, indicating that there is an extra mechanism. It is reasonable to introduce the dislocation viscous drag into the traditional Z-A model, and it is employed as follows [112]:

$$\sigma_y = \frac{\beta_0 \varepsilon^{1/2} \exp\left(-\beta_1 T + \beta_2 T \ln \dot{\varepsilon}\right)}{(1 - c\dot{\varepsilon})^{\beta_2 T}} + \sigma_0, \tag{4}$$

where c is a material parameter. The thermal-activation equation with dislocation drag [red thread in Fig. 11(a)] could better capture the strain-rate effect of σ_y upon high-speed loading in the current MEAs, and c is determined to be 2.31×10^{-4} s.

Similarly, the YSs of Q77 and D77 are approximately predicted, using Eq. (4), and they are 965 and 1103 MPa, respectively. The predicted results have 2.6 and 16.4% deviations from experimental values, respectively. On one hand, during the cryogenic tension, an extra deformation mechanism, twinning, prevails before yielding, and thus, it may have a positive effect on the enhancement of YS. On the other hand, the temperature-dependent YSs may be ignored because of the data for fitting from room-temperature tension. Consequently, the mismatch between the experimental results and theoretical predictions emerges. Further work is needed to exactly predict the YSs from different temperatures.

2. *Strain-rate-dependent strain hardening*

Upon dynamic loading for materials, three mechanisms are substantially popular: work hardening, strain-rate hardening, and thermal softening [111]. The first two generally trigger the increase of the isothermal flow stress, while thermal softening always decreases it. Upon plastic straining, the plastic energy is usually converted into the heat, and it may trigger thermal softening [114]. The average temperature rise can be calculated by the following equation:

$$\Delta T = T - T_0 = \int_{T_0}^{T} dT = \frac{\beta}{\rho C_p} \int_0^{\varepsilon_p} \sigma d\varepsilon_p, \tag{5}$$

where ΔT is the temperature rise, T is the instantaneous temperature, T_0 is the initial temperature, and it is considered as 298 K, ρ is the mass density, which is calculated to be 7.98 g cm^{-3}, C_p is the heat capacity, which is estimated to be 0.446 J g^{-1} K^{-1}, according to the rule of mixture [115]. Here, β is the fraction of the plastic energy converted to heat and chosen as 0.9 [53], and ε_p is the true plastic strain. Calculated by Eq. (5), the temperature rises of 26.3, 23.5, and 15.3 K are obtained at the strain rates of 2000, 3000, and 4000 s^{-1}, respectively, as shown in Fig. 12(a). Hence, thermal softening is reasonably ruled out upon high-speeding loading.

In this paper, a look at the microstructure evolution indicates that both dislocation strengthening and twinning strengthening contribute to work hardening. Based on Taylor's hardening model, a microstructure-based constitutive model would be developed. The stress induced by forest dislocations can be described by [116]

$$\sigma_f = M\alpha G b\sqrt{\rho}, \tag{6}$$

where M is the average Taylor factor, G is the shear modulus (taken as 69 GPa for current MEAs at 298 K [32]), α is a constant related to the dislocation interaction strength, and it is taken as 0.4 at 298 K [3], ρ is the total dislocation density, which is estimated to be 1.592×10^{13} m^{-2} (the detailed calculation can be found in the Supplemental Material [39,117]), and b is the Burgers vector for the perfect dislocation, which is taken as 0.254 nm [32]. The evolution of the total dislocation density considering the competition between the dislocation

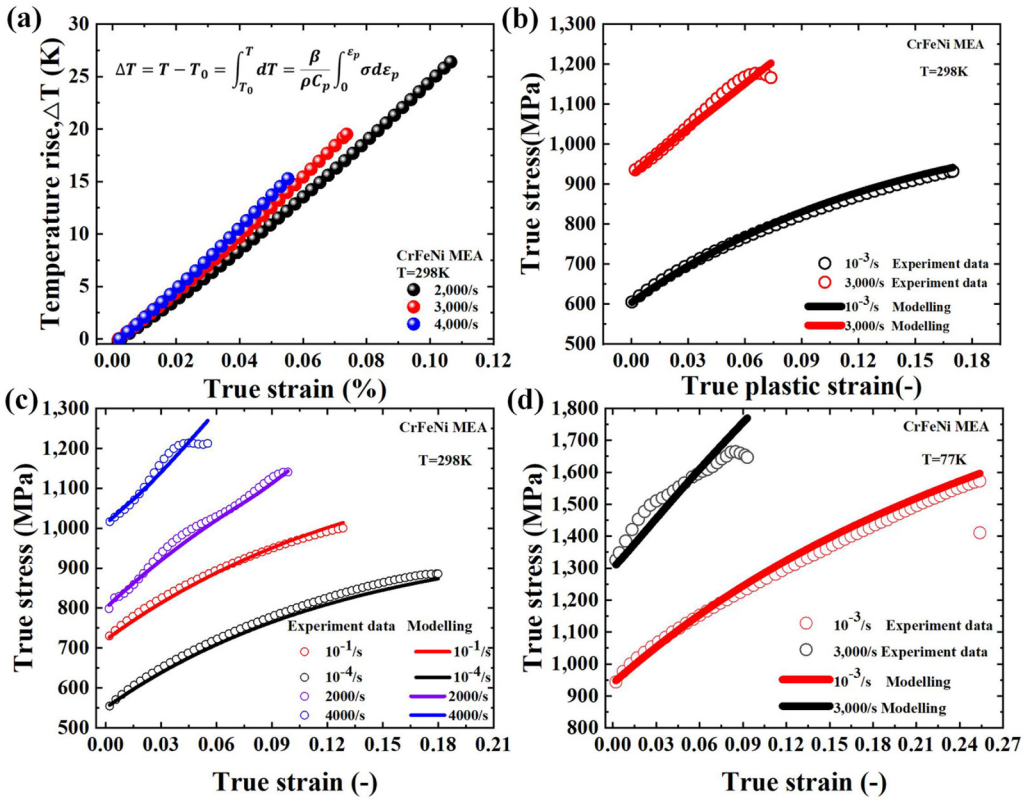

FIG. 12. (a) Adiabatic temperature rising of current CrFeNi medium entropy alloys (MEAs) under dynamic loading. (b) Experimental true stress after yielding of CrFeNi MEA and corresponding curves from best fitting. Experimental true stress after yielding and corresponding predicted results at (c) 298 K and (d) 77 K.

storage and recovery can be calculated as follows [118]:

$$\frac{d\rho}{d\varepsilon_p} = M\left(\frac{1}{b\Lambda} - k\rho\right), \tag{7}$$

where Λ is the mean free path, and the corresponding calculations are described below. Here, k is the dynamic recovery factor depending on the strain rate and temperature, which can be written as follows [119]:

$$k = k_0\left(\frac{\dot{\varepsilon}}{\dot{\varepsilon}_0}\right)^{-KT/A}. \tag{8}$$

Here, k_0 is a recovery factor at 0 K, and K is Boltzmann constant, which is $1.38 \times 10^{-23}\,\mathrm{J\,K^{-1}}$. Also, $\dot{\varepsilon}_0$ is the reference strain rate, and it is taken as $10^7\,\mathrm{s^{-1}}$ [119]. Further, T is the transient temperature during deformation, which is ignored since the calculated temperature rise is very small. Then A is a material parameter depending on the SFE (γ_{SFE}), and it can be calculated based on a phenomenological equation [120]:

$$\frac{A}{Gb^3} = \frac{1}{\exp(1.44 + 27.55\xi - 390.54\xi^2)}, \tag{9}$$

where ξ is the normalized SFE ($\xi = \gamma_{\mathrm{SFE}}/Gb$). Substituting the value of SFE, A is determined to be 2.4×10^{-19} J for the current MEAs at 298 K.

Based on the above microstructural observations (the twinning plays a vital role upon dynamic tension, while it is innocuous upon the quasistatic one), the only kinds of impenetrable obstacles to dislocation motion are those related to the dislocation structure itself for the current MEAs under the quasistatic tension. As a result, $1/\Lambda$ is proportional to $1/\sqrt{\rho}$ for the current alloys under quasistatic deformation, regardless of the dislocation operations—completely random or a cell or subgrain structure [60], i.e., $\Lambda = k_1\sqrt{\rho}$. In contrast, the nanotwin boundaries must be considered upon high-speed tension, i.e., $\Lambda = k_2\sqrt{\rho} + \frac{i_\Delta}{\Delta}$, with k_1 and k_2 being the relevant dislocation storage rates under quasistatic and dynamic conditions, respectively. Here, i_Δ is a constant for scaling the contribution of the average twin spacing to the effective boundary distance, which is taken as 0.14 for current alloys with reference to TWIP steels [120]. Also, Δ is the average twin spacing, which can be established from the stereological analysis by Fullman [121]:

$$\Delta = 2t\frac{1-F}{F}, \tag{10}$$

where t is the average twin thickness, and F is the twin volume fraction, and its evolution can be captured based on the equation of Olson and Cohen [72]:

$$F = 1 - \exp[-\varphi(\varepsilon_p - \varepsilon_{\mathrm{int}})], \tag{11}$$

where φ is a strain-independent constant, and $\varepsilon_{\mathrm{int}}$ is a twinning initial strain determined by the critical twinning stress (σ_{crit}). It is expected that φ is dependent on the SFE and strain rates, with an increase resulting from decreasing fault energies and/or increasing strain rates, since these factors tend to favor twinning rather than dislocation slip [72]. The critical stress required for twinning is estimated to be 1069 MPa upon

TABLE III. Material constants and parameters in the constitutive model.

	Description	Value
M	Taylor factor	3.06
G	Shear modulus	69 GPa (298 K) 76 GPa (77 K)
ρ_{int}	Initial dislocation density	2.254×10^{13} m^{-2}
α	Dislocation interaction strength	0.4
b	Burgers vector for perfect dislocation	0.254 nm
i_Δ	Scaling constant for twin spacing	0.14
C_v	Heat capacity	0.446 J g^{-1} K^{-1}
β	Plastic energy-heat conversion fraction	0.9
T_m	Melting temperature	1875 K
ρ	Mass density	7.98 g cm^{-3}
γ_{SF}	Stacking fault energy	65.85 mJ m^{-2} (298 K) 43.30 mJ m^{-2} (77 K)
T	Average twin thickness	2.5 nm (D298) 11.6 nm (Q77) 5.3 nm (D77)
φ	Material constant	0.653 (D298) 0.149 (Q77) 0.368 (D77)
K	Boltzmann constant	1.380649×10^{23}
A	Material parameter	2.43×10^{19} J 298 K 2.78×10^{19} J 77 K
$\dot{\varepsilon}_0$	Reference strain rate	10^7 s^{-1}
k_0	Athermal recovery factor	3.21
k_1	Dislocation hardening factor (S)	3.06×10^{-2}
k_2	Dislocation hardening factor (D)	3.59×10^{-2}

room-temperature quasistatic deformation. Also, the initial twinning strains take values of 7.4, 3.55, and 1.5% at strain rates of 2000, 3000, and 4000 s^{-1}, respectively. Combining the ε_{int} and the twin fraction experimentally obtained above, φ is calculated to be 0.653 at 298 K.

Therefore, the above Eqs. (6)–(11) fully describes the current constitutive relation of CrFeNi MEAs under quasistatic and dynamic tension at room temperature. All material constants and parameters used in the model are listed in Table III. Here, k_1, k_2, and k_0 are the parameters which are needed to be determined by fitting stress-strain curves. The fitting parameters from best fits are also summarized in Table III, and the corresponding model prediction and tested results are depicted in Fig. 12(b). The plastic flows at different strain rates are almost exactly predicted, using the parameters obtained by fitting, as shown in Fig. 12(c).

The model is further employed to predict the evolution of the flow stress with strain at 77 K by substituting the corresponding temperature into Eqs. (6)–(11). It is noted that many parameters in the above formula will change as the temperature varies. For example, shear modulus is a temperature-dependent constant and increases with decreasing the temperature. Due to limited reports on CrFeNi MEAs, the temperature dependence of shear modulus is lacking. Here, the shear modulus of the current CrFeNi MEA at 77 K is approximately estimated to be 1.1 times that at 298 K, i.e., 76 GPa at 77 K [17]. As described above, φ is a strain-rate- and SFE-dependent constant and determined from the initial twin strain and twin fraction. As listed in Sec. IV 1, the initial twinning strains are 0.7 and 0.2% for Q77 and D77, respectively. Combining ε_{int} and the twin fraction from the microstructure analysis, φ is 0.368 and 0.149 for D77 and Q77, respectively. The fitting results are displayed in Fig. 12(d), and the present constitutive model successfully predicts the flow stress behavior for D77. This constitutive equation captures the stress-strain curves of HEAs/MEAs under cryogenic temperatures.

Additionally, the Johnson-Cook (J-C) model is an empirical viscoplastic-constitutive model, which is widely employed to describe the macroscopic plastic-flow behavior of many different kinds of alloys under high strain rates [62,111]. Based on the J-C model, the relationships of the strain and stress are fitted, and the fitting results agree well with the experimental results, as presented in Fig. S4 in the Supplemental Material [39].

V. CONCLUSIONS

In this paper, the deformation behaviors of the CrFeNi MEA upon quasistatic and dynamic tension at room (298 K) and cryogenic (77 K) temperatures were investigated. The strain-rate and temperature dependences of deformation behaviors were modeled and discussed. By combining TEM and EBSD techniques, dislocation and twin substructures were carefully investigated to uncover microscopic deformation mechanisms. Based on our observations, the main findings are summarized as follows:

(1) After severe cryorolling and annealing at 800 °C for 1 h, the grain-size distribution of an FCC matrix is heterogeneous due to incomplete recrystallization during low-temperature annealing. Meanwhile, Cr-rich BCC precipitates were formed due to several aspects, including a VEC value of 8, high melting temperature, and large diffusion coefficient of Cr atoms compared with Fe and Ni atoms.

(2) With the temperature decrease from 298 to 77 K, both the strength and UE are significantly improved upon quasistatic and dynamic loadings, which is attributed to the activation of twins, causing a dynamic Hall-Petch effect.

(3) Under dynamic loading, a traditional strength-ductility tradeoff comes into being in the current CrFeNi MEA. The YS was significantly increased since the dislocation motion becomes popular under high strain-rate loading. High-density dislocations together with brittle BCC phases within the FCC matrix cause the reduction of UEs upon dynamic loading.

(4) The SRS of the CrFeNi MEA (m_s is 0.0371 under quasistatic loading, and m_d is 0.33968 under dynamic loading) is higher than that of pure FCC metals and complex solid-solution alloys, such as stainless steels, HEAs, and MEAs. The strong strain-rate dependence of the YS is closely related to the presence of short-range dislocation obstacles, BCC phases, and ultrafine grains.

(5) A strain-rate- and temperature-dependent constitutive model was well established to describe the deformation behaviors of the CrFeNi MEA over a wide range of strain rates from 10^{-4} to 4000 s^{-1} at room and cryogenic temperatures. The predicted results are in good accord with the experimental data.

ACKNOWLEDGMENTS

The authors would like to acknowledge the financial support of the Natural Science Foundation of Shanxi Province, China (No. 201901D111105 and No. 201901D111114), and the opening project of the State Key Laboratory of Explosion Science and Technology (Beijing Institute of Technology; No. KFJJ20-13M. P.K.L. very much appreciates the supports from (1) the U.S. National Science Foundation (No. DMR-1611180 and No. 1809640) with the program directors Dr. Judith Yang, Dr. Gary Shiflet, and Dr. Diana Farkas, and (2) the Army Office Project (No. W911NF-13-1-0438 and No. W911NF-19-2-0049) with the program managers Dr. Michael P. Bakas, Dr. David M. Stepp, and Dr. S. Mathaudhu.

The authors declare no competing financial interests.

[1] L. Tang, L. Wang, M. Wang, H. Liu, S. Kabra, Y. Chiu, and B. Cai, Synergistic deformation pathways in a TWIP steel at cryogenic temperatures: *in situ* neutron diffraction, Acta Mater. **200**, 943 (2020).

[2] S. S. Sohn, S. Hong, J. Lee, B. C. Suh, S. K. Kim, B. J. Lee, N. J. Kim, and S. Lee, Effects of Mn and Al contents on cryogenic-temperature tensile and Charpy impact properties in four austenitic high-Mn steels, Acta Mater. **100**, 39 (2015).

[3] T. W. Zhang, S. G. Ma, D. Zhao, Y. C. Wu, Y. Zhang, Z. H. Wang, and J. W. Qiao, Simultaneous enhancement of strength and ductility in a NiCoCrFe high-entropy alloy upon dynamic tension: micromechanism and constitutive modeling, Int. J. Plast. **124**, 226 (2020).

[4] B. Gludovatz, A. Hohenwarter, D. Catoor, E. H. Chang, E. P. George, and R. O. Ritchie, A fracture-resistant high-entropy alloy for cryogenic applications, Science **345**, 1153 (2014).

[5] Y. Tong, D. Chen, B. Han, J. Wang, R. Feng, T. Yang, C. Zhao, Y. L. Zhao, W. Guo, Y. Shimizu, C. T. Liu, P. K. Liaw, K. Inoue, Y. Nagai, A. Hu, and J. J. Kai, Outstanding tensile properties of a precipitation-strengthened $FeCoNiCrTi_{0.2}$ high-entropy alloy at room and cryogenic temperatures, Acta Mater. **165**, 228 (2019).

[6] S. Praveen and H. S. Kim, High-entropy alloys: potential candidates for high-temperature applications—an overview, Adv. Eng. Mater. **20**, 1700645 (2018).

[7] W. Li, D. Xie, D. Li, Y. Zhang, Y. Gao, and P. K. Liaw, Mechanical behavior of high-entropy alloys, Prog. Mater Sci. **118**, 100777 (2021).

[8] E. P. George, W. A. Curtin, and C. C. Tasan, High entropy alloys: a focused review of mechanical properties and deformation mechanisms, Acta Mater. **188**, 435 (2020).

[9] T. Yang, Y. L. Zhao, J. H. Luan, B. Han, J. Wei, J. J. Kai, and C. T. Liu, Nanoparticles-strengthened high-entropy alloys for cryogenic applications showing an exceptional strength-ductility synergy, Scripta Mater. **164**, 30 (2019).

[10] Z. Li, S. Zhao, R. O. Ritchie, and M. A. Meyers, Mechanical properties of high-entropy alloys with emphasis on face-centered cubic alloys, Prog. Mater Sci. **102**, 296 (2019).

[11] Y. Zhang, T. T. Zuo, Z. Tang, M. C. Gao, K. A. Dahmen, P. K. Liaw, and Z. P. Lu, Microstructures and properties of high-entropy alloys, Prog. Mater Sci. **61**, 1 (2014).

[12] Z. Wu, S. A. David, Z. Feng, and H. Bei, Weldability of a high entropy CrMnFeCoNi alloy, Scripta Mater. **124**, 81 (2016).

[13] M. A. Hemphill, T. Yuan, G. Y. Wang, J. W. Yeh, C. W. Tsai, A. Chuang, and P. K. Liaw, Fatigue behavior of $Al_{0.5}CoCrCuFeNi$ high entropy alloys, Acta Mater. **60**, 5723 (2012).

[14] K. Liu, S. S. Nene, M. Frank, S. Sinha, and R. S. Mishra, Extremely high fatigue resistance in an ultrafine grained high entropy alloy, Appl. Mater. Today **15**, 525 (2019).

[15] E. P. George, D. Raabe, and R. O. Ritchie, High-entropy alloys, Nat. Rev. Mater. **4**, 515 (2019).

[16] Y. Zhao, D. H. Lee, M. Y. Seok, J. A. Lee, M. P. Phaniraj, J. Y. Suh, H. Y. Ha, J. Y. Kim, U. Ramamurty, and J.-i. Jang, Resistance of CoCrFeMnNi high-entropy alloy to gaseous hydrogen embrittlement, Scripta Mater. **135**, 54 (2017).

[17] Z. Wu, H. Bei, G. M. Pharr, and E. P. George, Temperature dependence of the mechanical properties of equiatomic solid solution alloys with face-centered cubic crystal structures, Acta Mater. **81**, 428 (2014).

[18] D. B. Miracle and O. N. Senkov, A critical review of high entropy alloys and related concepts, Acta Mater. **122**, 448 (2017).

[19] J. Moon, J. M. Park, J. W. Bae, H.-S. Do, B.-J. Lee, and H. S. Kim, A new strategy for designing immiscible medium-entropy alloys with excellent tensile properties, Acta Mater. **193**, 71 (2020).

[20] D. G. Kim, Y. H. Jo, J. Yang, W. M. Choi, H. S. Kim, B. J. Lee, S. S. Sohn, and S. Lee, Ultrastrong duplex high-entropy alloy with 2 GPa cryogenic strength enabled by an accelerated martensitic transformation, Scripta Mater. **171**, 67 (2019).

[21] N. Kumar, Q. Ying, X. Nie, R. S. Mishra, Z. Tang, P. K. Liaw, R. E. Brennan, K. J. Doherty, and K. C. Cho, High strain-rate compressive deformation behavior of the $Al_{0.1}CrFeCoNi$ high entropy alloy, Mater. Des. **86**, 598 (2015).

[22] S. G. Ma, Z. M. Jiao, J. W. Qiao, H. J. Yang, Y. Zhang, and Z. H. Wang, Strain rate effects on the dynamic mechanical properties of the $AlCrCuFeNi_2$ high-entropy alloy, Mater. Sci. Eng., A **649**, 35 (2016).

[23] B. Wang, A. Fu, X. Huang, B. Liu, Y. Liu, Z. Li, and X. Zan, Mechanical properties and microstructure of the CoCrFeMnNi high entropy alloy under high strain rate compression, J. Mater. Eng. Perform. **25**, 2985 (2016).

[24] T. W. Zhang, Z. M. Jiao, Z. H. Wang, and J. W. Qiao, Dynamic deformation behaviors and constitutive relations of an $AlCoCr_{1.5}Fe_{1.5}NiTi_{0.5}$ high-entropy alloy, Scripta Mater. **136**, 15 (2017).

[25] J. M. Park, J. Moon, J. W. Bae, M. J. Jang, J. Park, S. Lee, and H. S. Kim, Strain rate effects of dynamic compressive deformation on mechanical properties and microstructure of CoCrFeMnNi high-entropy alloy, Mater. Sci. Eng., A **719**, 155 (2018).

[26] H. Song, D. G. Kim, D. W. Kim, M. C. Jo, Y. H. Jo, W. Kim, H. S. Kim, B. J. Lee, and S. Lee, Effects of strain rate on room- and cryogenic-temperature compressive properties in metastable $V_{10}Cr_{10}Fe_{45}Co_{35}$ high-entropy alloy, Sci. Rep. **9**, 6163 (2019).

[27] Z. Li, S. Zhao, H. Diao, P. K. Liaw, and M. A. Meyers, High-velocity deformation of $Al_{0.3}CoCrFeNi$ high-entropy

alloy: Remarkable resistance to shear failure, Sci. Rep. **7**, 42742 (2017).

[28] C. M. Cao, W. Tong, S. H. Bukhari, J. Xu, Y. X. Hao, P. Gu, H. Hao, and L. M. Peng, Dynamic tensile deformation and microstructural evolution of Al_xCrMnFeCoNi high-entropy alloys, Mater. Sci. Eng., A **759**, 648 (2019).

[29] Z. F. He, N. Jia, H. W. Wang, Y. Liu, D. Y. Li, and Y. F. Shen, The effect of strain rate on mechanical properties and microstructure of a metastable FeMnCoCr high entropy alloy, Mater. Sci. Eng., A **776**, 138982 (2020).

[30] J. He, Q. Wang, H. Zhang, L. Dai, T. Mukai, Y. Wu, X. Liu, H. Wang, T. G. Nieh, and Z. Lu, Dynamic deformation behavior of a face-centered cubic FeCoNiCrMn high-entropy alloy, Sci. Bull. **63**, 362 (2018).

[31] H. Kim, J. Park, Y. Ha, W. Kim, S. S. Sohn, H. S. Kim, B.-J. Lee, N. J. Kim, and S. Lee, Dynamic tension-compression asymmetry of martensitic transformation in austenitic Fe-(0.4, 1.0)C-18Mn steels for cryogenic applications, Acta Mater. **96**, 37 (2015).

[32] K. Wang, X. J. Wang, T. W. Zhang, X. Jin, H. J. Yang, and J. W. Qiao, Tuning Cr-rich nanoprecipitation and heterogeneous structure in equiatomic CrFeNi medium-entropy stainless alloys, J. Iron Steel Res. Int. (2021), doi: 10.1007/s42243-020-00520-y.

[33] W. R. Wang, W. L. Wang, S. C. Wang, Y. C. Tsai, C. H. Lai, and J. W. Yeh, Effects of Al addition on the microstructure and mechanical property of Al_xCoCrFeNi high-entropy alloys, Intermetallics **26**, 44 (2012).

[34] J. C. Rao, H. Y. Diao, V. Ocelík, D. Vainchtein, C. Zhang, C. Kuo, Z. Tang, W. Guo, J. D. Poplawsky, Y. Zhou, P. K. Liaw, and J. T. M. De Hosson, Secondary phases in Al_xCoCrFeNi high-entropy alloys: An *in-situ* TEM heating study and thermodynamic appraisal, Acta Mater. **131**, 206 (2017).

[35] F. Otto, A. Dlouhý, K. G. Pradeep, M. Kuběnová, D. Raabe, G. Eggeler, and E. P. George, Decomposition of the single-phase high-entropy alloy CrMnFeCoNi after prolonged anneals at intermediate temperatures, Acta Mater. **112**, 40 (2016).

[36] O Smuk, Y. Jagodzinski, O Tarasenko, S. Smuk, and H. Hanninen, Internal friction study of decomposition kinetics of SAF 2507 type duplex stainless steel, Scripta Mater. **40**, 321 (1999).

[37] S. Guo, C. Ng, J. Lu, and C. T. Liu, Effect of valence electron concentration on stability of fcc or bcc phase in high entropy alloys, J. Appl. Phys. **109**, 103505 (2011).

[38] X. Yang and Y. Zhang, Prediction of high-entropy stabilized solid-solution in multi-component alloys, Mater. Chem. Phys. **132**, 233 (2012).

[39] See Supplemental Material at http://link.aps.org/supplemental/10.1103/PhysRevMaterials.5.113608 for (1) calculation of dislocation density in undeformed samples; (2) calculation of SFE; (3) thermodynamic evaluations of the $Cr_x(FeNi)_{100-x}$ alloy systems; (4) SEM fractographs of tensile specimens; (5) XRD patterns of tensile specimens; (6) comparison of experimental and predicted true stress-strain relations from the modified J-C constitutive equations at different strain rates; (7) mechanical properties of current MEAs and some conventional metals/alloys at different strain rates and temperatures; and (8) SRS of CrFeNi MEAs and other representative FCC metals and alloys.

[40] K. Y. Tsai, M. H. Tsai, and J. W. Yeh, Sluggish diffusion in Co-Cr-Fe-Mn-Ni high-entropy alloys, Acta Mater. **61**, 4887 (2013).

[41] L. J. Santodonato, Y. Zhang, M. Feygenson, C. M. Parish, M. C. Gao, R. J. Weber, J. C. Neuefeind, Z. Tang, and P. K. Liaw, Deviation from high-entropy configurations in the atomic distributions of a multi-principal-element alloy, Nat. Commun. **6**, 5964 (2015).

[42] M. Yang, D. Yan, F. Yuan, P. Jiang, E. Ma, and X. Wu, Dynamically reinforced heterogeneous grain structure prolongs ductility in a medium-entropy alloy with gigapascal yield strength, Proc. Nati. Acad. Sci. USA **115**, 7224 (2018).

[43] Y. Li, Y. Lu, W. Li, M. Khedr, H. Liu, and X. Jin, Hierarchical microstructure design of a bimodal grained twinning-induced plasticity steel with excellent cryogenic mechanical properties, Acta Mater. **158**, 79 (2018).

[44] M. A. Meyers and K. K. Chawla, *Mechanical Behavior of Materials* (Cambridge University Press, Cambridge, 2009).

[45] M. Baig, A. S. Khan, S.-H. Choi, and A. Jeong, Shear and multiaxial responses of oxygen free high conductivity (OFHC) copper over wide range of strain-rates and temperatures and constitutive modeling, Int. J. Plast. **40**, 65 (2013).

[46] S. Nemat-Nasser, W. Guo, and M. Liu, Experimentally-based micromechanical modeling of dynamic response of molybdenum, Scripta Mater. **40**, 859 (1999).

[47] S. Nemat-Nasser and W. Guo, High strain-rate response of commercially pure vanadium, Mech. Mater. **32**, 243 (2000).

[48] S. Nemat-Nasser and W. Guo, Flow stress of commercially pure niobium over a broad range of temperatures and strain rates, Mater. Sci. Eng., A **284**, 202 (2000).

[49] R. Kapoor and S. Nemat-Nasser, Comparison between high and low strain-rate deformation of tantalum, Matall. Mater. Trans. A **31**, 815 (2000).

[50] M. Ardeljan, I. J. Beyerlein, B. A. McWilliams, and M. Knezevic, Strain rate and temperature sensitive multi-level crystal plasticity model for large plastic deformation behavior: application to AZ31 magnesium alloy, Int. J. Plast. **83**, 90 (2016).

[51] S. Curtze, V. T. Kuokkala, M. Hokka, and P. Peura, Deformation behavior of TRIP and DP steels in tension at different temperatures over a wide range of strain rates, Mater. Sci. Eng., A **507**, 124 (2009).

[52] M. Hokka, V. T. Kuokkala, and S. Curtze, Dynamic tensile behaviour of TRIP and DP steels at different temperatures, Steel Res. Int. **80**, 137 (2009).

[53] W. G. Guo and S. Nemat Nasser, Flow stress of Nitronic-50 stainless steel over a wide range of strain rates and temperatures, Mech. Mater. **38**, 1090 (2006).

[54] F. Abed and G. Voyiadjis, Plastic deformation modeling of AL-6XN stainless steel at low and high strain rates and temperatures using a combination of bcc and fcc mechanisms of metals, Int. J. Plast. **21**, 1618 (2005).

[55] J. Zhang and Y. Wang, Effect of strain rate on the tension behavior of Ti-6.6Al-3.3Mo-1.8Zr-0.29Si alloy at low temperatures, Mater. Sci. Eng., A **605**, 59 (2014).

[56] R. U. Vaidya, Z. Jin, C. Cady, G. T. G. Iii, and D. P. Butt, A comparative study of the strain rate and temperature dependent compression behavior of Ti-46.5Al-3Nb-2Cr-0.2W and Ti-25Al-10Nb-3V-1Mo intermetallic alloys, Scripta Mater. **41**, 569 (1999).

[57] J. Wang, W.-G. Guo, X. Gao, and J. Su, The third-type of strain aging and the constitutive modeling of a Q235B steel over a wide range of temperatures and strain rates, Int. J. Plast. **65**, 85 (2015).

[58] J. Ding, Q. Yu, M. Asta, and R. O. Ritchie, Tunable stacking fault energies by tailoring local chemical order in CrCoNi medium-entropy alloys, Proc, Nat. Acad. Sci. USA **115**, 8919 (2018).

[59] G. Bonny, N. Castin, and D. Terentyev, Interatomic potential for studying ageing under irradiation in stainless steels: the FeNiCr model alloy, Modell. Simul. Mater. Sci. Eng. **21**, 5897 (2013).

[60] H. Kim, M. Kang, H. J. Jung, H. S. Kim, and S. Lee, Mechanisms of toughness improvement in Charpy impact and fracture toughness tests of non-heat-treating cold-drawn steel bar, Mater. Sci. Eng., A **571**, 38 (2013).

[61] W. S. Lee and C. F. Lin, Impact properties and microstructure evolution of 304L stainless steel, Mater. Sci. Eng., A **308**, 124 (2001).

[62] L. Wang, J. W. Qiao, S. G. Ma, Z. M. Jiao, T. W. Zhang, G. Chen, D. Zhao, Y. Zhang, and Z. H. Wang, Mechanical response and deformation behavior of $Al_{0.6}$CoCrFeNi high-entropy alloys upon dynamic loading, Mater. Sci. Eng., A **727**, 208 (2018).

[63] Z. Wang, W. Lu, H. Zhao, C. H. Liebscher, and Z. Li, Ultrastrong lightweight compositionally complex steels via dual-nanoprecipitation, Sci. Adv. **6**, 9543 (2020).

[64] M. Bönisch, Y. Wu, and H. Sehitoglu, Twinning-induced strain hardening in dual-phase FeCoCrNi$Al_{0.5}$ at room and cryogenic temperature, Sci. Rep. **8**, 10663 (2018).

[65] R. P. Reed, The spontaneous martensitic transformations in 18% Cr, 8% Ni steels, Acta Metall. **10**, 865 (1962).

[66] D. Wei, X. Li, S. Schönecker, J. Jiang, W. M. Choi, B. J. Lee, H. S. Kim, A. Chiba, and H. Kato, Development of strong and ductile metastable face-centered cubic single-phase high-entropy alloys, Acta Mater. **181**, 318 (2019).

[67] S. Zhao, Z. Li, C. Zhu, W. Yang, Z. Zhang, D. E. J. Armstrong, P. S. Grant, R. O. Ritchie, and M. A. Meyers, Amorphization in extreme deformation of the CrMnFeCoNi high-entropy alloy, Sci. Adv. **7**, 3108 (2021).

[68] K. Ming, W. Lu, Z. Li, X. Bi, and J. Wang, Amorphous bands induced by low temperature tension in a non-equiatomic CrMnFeCoNi alloy, Acta Mater. **188**, 354 (2020).

[69] G. Laplanche, A. Kostka, C. Reinhart, J. Hunfeld, G. Eggeler, and E. P. George, Reasons for the superior mechanical properties of medium-entropy CrCoNi compared to high-entropy CrMnFeCoNi, Acta Mater. **128**, 292 (2017).

[70] J. Lu, L. Hultman, E. Holmström, K. H. Antonsson, M. Grehk, W. Li, L. Vitos, and A. Golpayegani, Stacking fault energies in austenitic stainless steels, Acta Mater. **111**, 39 (2016).

[71] Y. Wang, B. Liu, K. Yan, M. Wang, S. Kabra, Y.-L. Chiu, D. Dye, P. D. Lee, Y. Liu, and B. Cai, Probing deformation mechanisms of a FeCoCrNi high-entropy alloy at 293 and 77 K using in situ neutron diffraction, Acta Mater. **154**, 79 (2018).

[72] G. B. Olson and M. Cohen, Kinetics of strain-induced martensitic nucleation, Matall. Mater. Trans. A **6**, 791 (1975).

[73] S. Curtze, V. T. Kuokkala, A. Oikari, J. Talonen, and H. Hänninen, Thermodynamic modeling of the stacking fault energy of austenitic steels, Acta Mater. **59**, 1068 (2011).

[74] S. Allain, J. P. Chateau, O. Bouaziz, S. Migot, and N. Guelton, Correlations between the calculated stacking fault energy and the plasticity mechanisms in Fe-Mn-C alloys, Mater. Sci. Eng., A **158** 387 (2004).

[75] I. A Yakubtsov, A Ariapour, and D. D. Perovic, Effect of nitrogen on stacking fault energy of f.c.c. iron-based alloys, Acta Mater. **47**, 1271 (1999).

[76] C. G. Rhodes and A. W. Thompson, The composition dependence of stacking fault energy in austenitic stainless steels, Matall. Mater. Trans. A **8**, 1901 (1977).

[77] K. Ishieda, Direct estimation of stacking fault energy by thermodynamic analysis, Phys. Status Solidi A **36**, 717 (1976).

[78] B. J. Lee, A thermodynamic evaluation of the Cr-Mn and Fe-Cr-Mn systems, Matall. Mater. Trans. A **24A**, 1919 (1993).

[79] L. Meng, P. Yang, Q. Xie, H. Ding, and Z. Tang, Dependence of deformation twinning on grain orientation in compressed high manganese steels, Scripta Mater. **56**, 931 (2007).

[80] M. A Meyers, O Vohringer, and V. A. Lubarda, The onset of twinning in metals: A constitutive description, Acta Mater. **49**, 4025 (2001).

[81] J. W. Christian and S. Mahajant, Deformation twinning, Prog. Mater Sci. **39**, 1 (1995).

[82] S. Curtze and V. T. Kuokkala, Dependence of tensile deformation behavior of TWIP steels on stacking fault energy, temperature and strain rate, Acta Mater. **58**, 5129 (2010).

[83] Y. H. Jo, S. Jung, W. M. Choi, S. S. Sohn, H. S. Kim, B. J. Lee, N. J. Kim, and S. Lee, Cryogenic strength improvement by utilizing room-temperature deformation twinning in a partially recrystallized VCrMnFeCoNi high-entropy alloy, Nat. Commun. **8**, 15719 (2017).

[84] G. Laplanche, A. Kostka, O. M. Horst, G. Eggeler, and E. P. George, Microstructure evolution and critical stress for twinning in the CrMnFeCoNi high-entropy alloy, Acta Mater. **118**, 152 (2016).

[85] D. R. Steinmetz, T. Jäpel, B. Wietbrock, P. Eisenlohr, I. Gutierrez-Urrutia, A. Saeed-Akbari, T. Hickel, F. Roters, and D. Raabe, Revealing the strain-hardening behavior of twinning-induced plasticity steels: Theory, simulations, experiments, Acta Mater. **61**, 494 (2013).

[86] T. S. Byun, On the stress dependence of partial dislocation separation and deformation microstructure in austenitic stainless steels, Acta Mater. **51**, 3063 (2003).

[87] W. Woo, J. S. Jeong, D. K. Kim, C. M. Lee, S. H. Choi, J. Y. Suh, S. Y. Lee, S. Harjo, and T. Kawasaki, Stacking fault energy analyses of additively manufactured stainless steel 316L and CrCoNi medium entropy alloy using *in situ* neutron diffraction, Sci. Rep. **10**, 1350 (2020).

[88] I. Gutierrez-Urrutia and D. Raabe, Dislocation and twin substructure evolution during strain hardening of an Fe-22 wt. % Mn-0.6 wt. % C TWIP steel observed by electron channeling contrast imaging, Acta Mater. **59**, 6449 (2011).

[89] P. Larour, P. Verleysen, K. Dahmen, and W. Bleck, Strain rate sensitivity of pre-strained AISI 301LN2B metastable austenitic stainless steel, Steel Res. Int. **84**, 72 (2013).

[90] Y. H. Jo, D. G. Kim, M. C. Jo, K. Y. Doh, S. S. Sohn, D. Lee, H. S. Kim, B. J. Lee, and S. Lee, Effects of deformation-induced BCC martensitic transformation and twinning on impact toughness and dynamic tensile response in metastable VCrFeCoNi high-entropy alloy, J. Alloys Compd. **785**, 1056 (2019).

[91] R. Bobbili and V. Madhu, A modified Johnson-Cook model for FeCoNiCr high entropy alloy over a wide range of strain rates, Mater. Lett. **218**, 103 (2018).
[92] R. W. Armstrong and S. M. Walley, High strain rate properties of metals and alloys, Int. Mater. Rev. **53**, 105 (2008).
[93] Y. L. S. Netat-Nasser, Flow stress of f.c.c. polycrystals with application to OFHC Cu, Acta Mater. **46**, 565 (1998).
[94] A. S. Khan and R. Liang, Behaviors of three BCC metal over a wide range of strain rates and temperatures: Experiments and modeling, Int. J. Plast. **15**, 1089 (1999).
[95] J. A. Lichtenfeld, M. C. Mataya, and C. J. V. Tyne, Effect of strain rate on stress-strain behavior of alloy 309 and 304L austenitic stainless steel, Matall. Mater. Trans. A **37A**, 147 (2006).
[96] W. S. Lee, C. F. Lin, and T. J. Liu, Strain rate dependence of impact properties of sintered 316L stainless steel, J. Nucl. Mater. **359**, 247 (2006).
[97] L. K. O. Grassel, G. Frommeyer, and L. W. Meyer, High strength Fe ± Mn ± (Al, Si) TRIP/TWIP steels development-properties-application, Int. J. Plast. **16**, 1391 (2000).
[98] G. Dirras, H. Couque, L. Lilensten, A. Heczel, D. Tingaud, J. P. Couzinié, L. Perrière, J. Gubicza, and I. Guillot, Mechanical behavior and microstructure of $Ti_{20}Hf_{20}Zr_{20}Ta_{20}Nb_{20}$ high-entropy alloy loaded under quasi-static and dynamic compression conditions, Mater. Charact. **111**, 106 (2016).
[99] Y. F. Xue, H. N. Cai, L. Wang, F. C. Wang, and H. F. Zhang, Effect of loading rate on failure in Zr-based bulk metallic glass, Mater. Sci. Eng., A **473**, 105 (2008).
[100] M. C. Li, M. Q. Jiang, S. Yang, F. Jiang, L. He, and J. Sun, Effect of strain rate on yielding strength of a Zr-based bulk metallic glass, Mater. Sci. Eng., A **680**, 21 (2017).
[101] R. S. Mishra, N. Kumar, and M. Komarasamy, Lattice strain framework for plastic deformation in complex concentrated alloys including high entropy alloys, Mater. Sci. Technol. **31**, 1259 (2015).
[102] C. Lee, G. Song, M. C. Gao, R. Feng, P. Chen, J. Brechtl, Y. Chen, K. An, W. Guo, J. D. Poplawsky, S. Li, A. T. Samaei, W. Chen, A. Hu, H. Choo, and P. K. Liaw, Lattice distortion in a strong and ductile refractory high-entropy alloy, Acta Mater. **160**, 158 (2018).
[103] C. Lee, Y. Chou, G. Kim, M. C. Gao, K. An, J. Brechtl, C. Zhang, W. Chen, J. D. Poplawsky, G. Song, Y. Ren, Y.-C. Chou, and P. K. Liaw, Lattice-distortion-enhanced yield strength in a refractory high-entropy alloy, Adv. Mater. **32**, 2004029 (2020).
[104] B. Yin, S. Yoshida, N. Tsuji, and W. A. Curtin, Yield strength and misfit volumes of NiCoCr and implications for short-range-order, Nat. Commun. **11**, 2507 (2020).
[105] Q. Ding, Y. Zhang, X. Chen, X. Fu, D. Chen, S. Chen, L. Gu, F. Wei, H. Bei, Y. Gao, M. Wen, J. Li, Z. Zhang, T. Zhu, R. O. Ritchie, and Q. Yu, Tuning element distribution, structure and properties by composition in high-entropy alloys, Nature (London) **574**, 223 (2019).
[106] M. Komarasamy, N. Kumar, R. S. Mishra, and P. K. Liaw, Anomalies in the deformation mechanism and kinetics of coarse-grained high entropy alloy, Mater. Sci. Eng., A **654**, 256 (2016).
[107] Q. Zhang, J. Zhang, and Y. Wang, Effect of strain rate on the tension-compression asymmetric responses of Ti-6.6Al-3.3Mo-1.8Zr-0.29Si, Mater. Des. **61**, 281 (2014).
[108] J. Tao, B. Gu, L. Chen, and J. Zhou, Tension-compression asymmetry of commercially pure titanium: Strain rate sensitivity and microstructure evolution, JOM **71**, 2280 (2019).
[109] W. D. Liu and K. X. Liu, Notable internal thermal effect on the yielding of metallic glasses, Appl. Phys. Lett. **100**, 141904 (2012).
[110] J. L. Dong, T. W. Zhang, Z. Wang, X. H. Shi, J. W. Qiao, Z. H. Wang, and Y. C. Wu, Homogeneous elongation and distinguishing work hardening in La-based metallic glass composites upon dynamic tension, Mater. Sci. Eng., A **736**, 329 (2018).
[111] M. A. Meyers, *Dynamic Behavior of Materials* (John Wiley and Sons, New York, 1994).
[112] F. J. Zerilli and R. W. Armstrong, The effect of dislocation drag on the stress-strain behavior of f.c.c. metals, Acta Metall. **40**, 1803 (1992).
[113] F. J. Zerilli and R. W. Armstrong, Dislocation-mechanics-based constitutive relations for material dynamics calculations, J. Appl. Phys. **61**, 1816 (1987).
[114] C. Zener and J. H. Hollomon, Effect of strain rate upon plastic flow of steel, J. Appl. Phys. **15**, 22 (1944).
[115] J. I. Lee, H. S. Oh, and E. S. Park, Manipulation of σ_y/κ ratio in single phase FCC solid-solutions, Appl. Phys. Lett. **109**, 061906 (2016).
[116] T. H. Courtney, *Mechanical Behavior of Materials* (McGraw-Hill Press, Waveland, 2004).
[117] S. W. Wu, G. Wang, Q. Wang, Y. D. Jia, J. Yi, Q. J. Zhai, J. B. Liu, B. A. Sun, H. J. Chu, J. Shen, P. K. Liaw, C. T. Liu, and T. Y. Zhang, Enhancement of strength-ductility trade-off in a high-entropy alloy through a heterogeneous structure, Acta Mater. **165**, 444 (2019).
[118] Y. Estrin, *Dislocation-Density-Related Constitutive Modeling* (Academic Pressed, San Diego, 1996).
[119] U. F. Kocks and H. Mecking, Physics and phenomenology of strain hardening: The FCC case, Prog. Mater Sci. **48**, 171 (2003).
[120] Z. Y. Liang, X. Wang, W. Huang, and M. X. Huang, Strain rate sensitivity and evolution of dislocations and twins in a twinning-induced plasticity steel, Acta Mater. **88**, 170 (2015).
[121] R. L. Fullman, Measurement of particle sizes in opaque bodies, JOM **5**, 447 (1953).

Correction: A footnote for the first author was inserted in error during the production process and has been removed. The format of the footnote for the last author has been fixed.